arXiv:1601.04525v2 [astro-ph.GA] 7 Sep 2016

The formation of the primitive star SDSS J102915+172927: effect of the dust mass and the grain-size distribution.

S. Bovino[1,2], T. Grassi[3], D. R. G. Schleicher[4], and R. Banerjee[1]
[1]*Hamburger Sternwarte, Universität Hamburg, Gojenbergsweg 112, 21029 Hamburg, Germany*
[2]*Kavli Institute for Theoretical Physics, University of California, Santa Barbara, California 93106, USA*
[3]*Niels Bohr Institute & Centre for Star and Planet Formation, Øster Voldgade 5-7, DK-1350 Copenhagen, Denmark*
[4]*Departamento de Astronomía, Facultad Ciencias Físicas y Matemáticas, Universidad de Concepción, Av. Esteban Iturra s/n Barrio Universitario, Casilla 160, Concepción, Chile*
stefano.bovino@uni-hamburg.de

ABSTRACT

Understanding the formation of the extremely metal poor star SDSS-J102915+172927 is of fundamental importance to improve our knowledge on the transition between the first and second generation of stars in the Universe. In this paper, we perform three-dimensional cosmological hydrodynamical simulations of dust-enriched halos during the early stages of the collapse process including a detailed treatment of the dust physics. We employ the astrochemistry package KROME coupled with the hydrodynamical code ENZO assuming grain size distributions produced by the explosion of core-collapse supernovae of 20 and 35 $M_\odot$ primordial stars which are suitable to reproduce the chemical pattern of the SDSS-J102915+172927 star. We find that the dust mass yield produced from Population III supernovae explosions is the most important factor which drives the thermal evolution and the dynamical properties of the halos. Hence, for the specific distributions relevant in this context, the composition, the dust optical properties, and the size-range have only minor effects on the results due to similar cooling functions. We also show that the critical dust mass to enable fragmentation provided by semi-analytical models should be revised, as we obtain values one order of magnitude larger. This determines the transition from disk fragmentation to a more filamentary fragmentation mode, and suggests that likely more than one single supernova event or efficient dust growth should be invoked to get such a high dust content.

Subject headings: stars: low-mass — stars: formation — methods: numerical — hydrodynamics

1. Introduction

The discovery of the extremely metal poor star SDSS J102915+172927 (Caffau et al. 2011) has opened the possibility to indirectly probe the conditions of primordial clouds and to explore the environments which have led to the transition between the first (PopIII) and the second generation of stars. The so called "Caffau's star" is in fact characterized by an extremely low metallicity of 4.5×10^{-5} $Z_\odot$, supposedly formed from a mini-halo enriched with dust and metals by the explosion of a massive primordial star (Klessen et al. 2012; Schneider et al. 2012b). From the observed abundances of Caffau's star it has been inferred that the supernova progenitor should have a mass of 20-40 $M_\odot$ which during the explosion released a content of dust of 0.01-0.4 $M_\odot$ in the medium (Schneider et al. 2012b). However, the mechanism that likely led to the formation of Caffau's star is far from being well-understood, because the interplay between different processes makes the problem rather intricate, both physically and numerically. Compared to the formation of PopIII stars,

where the chemistry is simple, for the second generation of stars the presence of dust, metals, and feedback adds complexity which results in a high computational cost and large uncertainties. Recently, Smith et al. (2015) performed cosmological simulations of a collapsing minihalo enriched by dust and metals obtained from the outcome of a supernova (SN) explosion of a 30 $M_\odot$ PopIII star. The outcome of the SN produced a uniform metallicity of $\sim 2\times10^{-5} Z_\odot$, and the collapse led to vigorous fragmentation and a turbulent density structure. However, their dust model assumes quantities averaged on a standard size distribution[1]. In addition, the amount of dust and the composition resemble the present-day ISM properties re-scaled by the metallicity, which is known to have a high depletion efficiency $f_{\rm dep}$, i.e. a significant amount of metals is locked into dust (Pollack et al. 1994). On the contrary, realistic models of dust grains formed in PopIII core-collapse SNe reported over the last decade (Todini & Ferrara 2001; Nozawa et al. 2007; Schneider et al. 2006, 2012b; Marassi et al. 2015) show very different grain size distributions and compositions, and much lower depletion efficiencies. This is also supported by recent observations of damped Ly-α systems with a metallicity $\sim 10^{-3} Z_\odot$ (Schady et al. 2010; Zafar et al. 2011). In previous studies Dopcke et al. (2011, 2013), starting from an idealized setup, employed a dust model similar to Smith et al. (2015) and explored different metallicities obtaining, through a sink particle algorithm, the mass distribution of the resulting protostellar clumps, which showed a transition from a flat to a peaky distribution with increasing metallicity. So far these are the first and the only works where the dust cooling has been included in three-dimensional (3D) simulations of gravitational collapse of a minihalo, but a comparison between the two studies is difficult as the initial conditions and the numerical code employed are very different.

In a recently submitted paper, Chiaki et al. (2016) employed a comprehensive chemical model coupled with a proper treatment of the dust grains including the grain growth. They performed simulations of collapsing halos starting from a cosmological initial setup obtained by the outcome of the Hirano et al. (2014) simulations suite. The fragmentation process has been studied assuming an adiabatic collapse for densities above 10^{16} cm^{-3} and they concluded that the fragmentation is strongly related to the metallicity of the gas, but also influenced by the collapse time-scale.

Even if this study is very detailed and includes a proper model for the dust grains, there are two important questions which have not been addressed: what is the effect of the grain size distribution and of different dust compositions on the thermal evolution and the dynamical properties of the collapsing halo? How does the dust mass yield affect the fragmentation? In this work we provide a quantitative study of the effect of different grain size distributions/compositions on the dynamics of collapsing minihalos enriched by dust for the case of SDSS J102915+172927, starting from cosmological initial conditions and allowing for a high dynamical resolution.

In the following sections we introduce the different grain size distributions employed in this work, and give the details of our numerical setup. Then we discuss the main results and draw our conclusions.

2. Numerical methods

2.1. Chemistry and microphysics

Chemistry, microphysics, and dust-related processes are treated via the KROME package[2] (Grassi et al. 2014), which is well suited to accurately and efficiently model chemistry and microphysics in hydrodynamical simulations. The package has been employed to study a variety of astrophysical problems, with a wide range of physical and chemical conditions (Bovino et al. 2014; Prieto et al. 2015; Katz et al. 2015; Schleicher et al. 2016), including the formation of supermassive black holes (Latif et al. 2014, 2015) and simulations of star-forming filaments (Seifried & Walch 2015).

In this work, we employ a state-of-the-art primordial network, together with the main cooling/heating processes needed to model the collapse of a metal-free minihalo. Specifically, we include: atomic and Compton cooling as adopted from Cen (1992), H_2 roto-vibrational cooling updated to Glover (2015), collisionally induced emis-

[1] See Klessen & Glover (2014) for an analysis of the inaccuracy and uncertainties of this approach.

[2] www.kromepackage.org

sion cooling (Grassi et al. 2014), and dust cooling (Sect. 2.2). Chemical heating and cooling produced by the formation/destruction of molecular hydrogen is also considered, these include the energy released by the formation of H_2 on dust (Hollenbach & McKee 1979), that we compute employing the size-dependent rates of Cazaux & Spaans (2009)[3]. The choice to not include metals is dictated by the fact that at this low metallicity the fine-structure metal cooling is negligible as we are well below the critical metallicity ($Z = 10^{-3.5} Z_\odot$) postulated by Bromm et al. (2001), and recently confirmed with high-resolution numerical simulations (Bovino et al. 2014).

2.2. Grain size distributions

We explore the effect of the grain size distribution following two different approaches. First, we employ the distribution and dust composition as expected from the outcome of core-collapse SNe explosion (Limongi & Chieffi 2012), which is reprocessed by a nucleation model (Schneider et al. 2012b; Chiaki et al. 2014). The SN models have been selected to reproduce the average elemental abundances of Caffau's star. These include six different grain species, namely amorphous carbon (AC), alumina (Al_2O_3), magnetite (Fe_3O_4), enstatite ($MgSiO_3$), forsterite (Mg_2SiO_4), and silica (SiO_2), with a distribution similar to the one reported in Fig. 2 of Chiaki et al. (2014), and take into account the passage of a reverse shock which can destroy the initial distribution produced by the SN. We consider here the case of a 35 $M_\odot$ progenitor star (run2 in Table 1) where the distribution (reported in Fig. 1) is affected by a weak reverse shock (labelled rev1 in Table 1) with a depletion factor $f_{\rm dep} = 0.0082$, and a case where the progenitor is a primordial star of 20 $M_\odot$ (run3) exposed to a stronger reverse shock (rev2 in Table 1), with a higher depletion factor, $f_{\rm dep} = 0.015$. We note that, due to the lack of details in previous papers, it is difficult to retrieve the grain-size distributions for every case. We therefore assume that the grain-size distribution shape is similar and we only change the dust mass yield ($f_{\rm dep}$) for the case with 20 $M_\odot$ (run2). As we will show in the next sections this is a good approximation as the shape of the distribution and the grain composition have only a minor impact on the final results. This was also shown by Ji et al. (2014) within a simple one-zone framework.

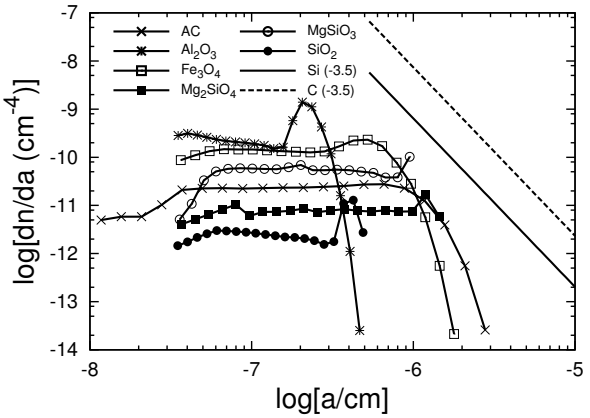

Fig. 1.— Dust grain distributions employed in this work. SN distributions with $f_{\rm dep} = 0.0082$ for different dust species, and the standard power-law distributions for C and Si.

Schneider et al. (2012b) postulated that to have fragmentation at the metallicity of Caffau's star $f_{\rm dep}$ should be larger than 0.01. This threshold has been obtained from simple one-zone models that may not capture the full 3D dynamics and should thus be considered with caution, as also discussed in Safranek-Shrader et al. (2014). With these two distributions we are able to explore values around (run2 and run3) and well above (run4 and run5) the threshold suggested by Schneider et al. (2012b) to see under which conditions it has a substantial impact on the density structure.

A second series of runs is performed including a typical power-law size distribution ($dn/da \propto a^{-\alpha}$), with exponent α = -3.5 (Mathis et al. 1977), where we assume a mix of carbonaceous and silicates resembling the Milky Way (MW) typical composition, with $a_{\rm min} = 5{\times}10^{-7}$ and $a_{\rm max} = 10^{-5}$ cm as reported in Fig. 1. We see that the power-law case has a high mass content ($f_{\rm dep} = 0.49$ as provided by Pollack et al. 1994 and also reported by Schneider et al. 2012a) and spans a smaller size-range. On the other hand, the distribution produced by SN models flattens at smaller radii as an effect of the reverse shock and extends down to very small sizes, of the order of 10^{-8} cm. These differences are relevant to un-

[3]The KROME setup employed in these simulations and the dust tables will be available on request.

derstand the thermodynamics of the system and the results we report in the next sections. In the case of the power-law (run7), we have to re-scale the solar dust-to-gas ratio by the star's metallicity $Z = 4.5 \times 10^{-5} Z_{\odot}$. As we aim to study the conditions under which Caffau's star was formed we employ the above fixed metallicity value for all the runs presented in this work.

Finally, we also run a case (run6) where we adopt the 35 $M_{\odot}$ model, but increase the depletion factor from 0.0082 to 0.49, i.e. assuming the same $f_{\rm dep}$ as for the power-law case, to disentangle the effect of the dust mass, composition, and distribution on the dynamics.

The dust physics is employed in KROME via look-up tables obtained by the procedure described in Grassi et al. (2016), which are only functions of the total density $n_{\rm tot}$ and the gas temperature T. We assume $N_d = 20$ bins in size per each grain type (N_t), which ensure a very good convergence on the results[4]. The total dust cooling is given by summing the contributions over all bins ($N_d \times N_t$) as

$$\Lambda_{\rm d} = \sum_{i=1}^{N_d \times N_t} \Lambda_{{\rm d},i} \,, \tag{1}$$

with

$$\Lambda_{{\rm d},i} = 2 f v_g n_g \pi L_i \,, \tag{2}$$

where v_g is the gas thermal speed, and f takes into account the contributions of species other than protons and is assumed to be equal to 0.5 (Hollenbach & McKee 1979). The term L_i is defined as

$$L_i = a_i^2 n_{d,i} k_B \left[T - T_{d,i}\right] \,, \tag{3}$$

where k_B is the Boltzmann constant, T the gas temperature, $n_{d,i}$, a_i, and $T_{d,i}$, are the dust number density, the grain size, and the dust temperature in the ith bin, respectively. The $N_d \times N_t$ dust temperatures are the roots of the non-linear system of equations

$$\beta_e(\mathbf{T}_d) \left[\Gamma_{em,i} - \Gamma_{abs,i}\right] = \Lambda_{{\rm d},i} \,, \tag{4}$$

where $i = 1, N_d \times N_t$, $\Gamma_{em,i}$, and $\Gamma_{abs,i}$ being the radiation emitted and absorbed by a dust grain, and β_e the escape probability (Omukai 2000) defined as

$$\beta_e(\mathbf{T}_d) = \min\left[1,\, (\tau_g + \tau_d)^{-2}\right] \,. \tag{5}$$

The gas opacity (τ_g) is taken from Mayer & Duschl (2005), while the optical constants for every individual dust species (τ_d) are obtained from the refractive indexes reported by the Jena Database (`www.astro.uni-jena.de/Laboratory/OCDB/`). For the carbonaceous and silicates employed in the power-law distribution, the optical constants are from Bruce Draine's website[5] (see Draine et al. 1984). The bulk densities are from Nozawa et al. (2006). We note here that β_e includes contributions from all dust bins and their respective temperatures ($\mathbf{T}_d = \{T_{d,1}, \ldots, T_{d,N_d \times N_t}\}$), thus making the system in Eq. 4 non-linear (see Grassi et al. 2016 for additional details).

3. Simulation setup

We select two minihalos of masses 10^6 $M_{\odot}$ and $7{\times}10^5$ $M_{\odot}$ and follow the collapse from cosmological initial conditions by employing the hydrodynamical code ENZO (Bryan et al. 2014). These minihalos have different properties and start to collapse at different times, $z = 22$ and $z = 18$, respectively (Latif et al. 2013; Bovino et al. 2014).

From $z = 99$ to $z = 22$ we evolve the halos to reach a central temperature of $\sim 10^3$ K at a density of $\sim 10^{-23}$ g cm^{-3} and then enable the dust machinery. Radiative and mechanical feedback from the previous generation of stars is neglected here and the dust mass fraction is constant during the evolution as we are not considering any process which might form or destroy dust but evaporation. We allow for 29 levels of refinement, which yield a resolution at a sub-AU level, and resolve the Jeans length by 64 cells. Our refinement strategy is based on over-density, Jeans length and particle mass and is applied during the simulations to ensure that all physical processes are well resolved and the Truelove criterion (Truelove et al. 1997; Federrath et al. 2011) is fulfilled. A summary of our runs is reported in Table 1. We

[4] Note that an acceptable convergence is already reached for 10 bins.

[5] `http://www.astro.princeton.edu/~draine/dust/dust.diel.html`

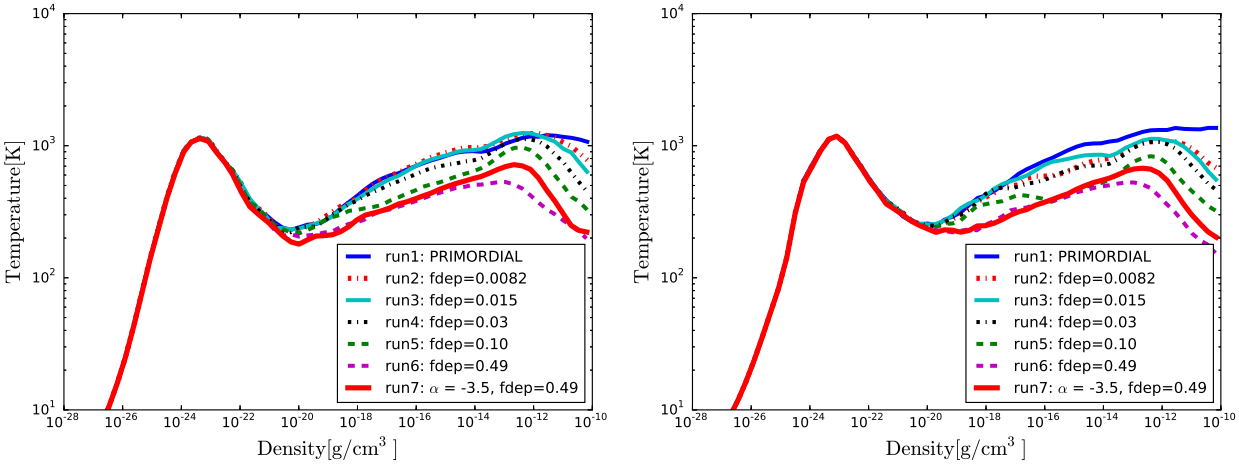

Fig. 2.— Profile of the mass-weighted average temperatures for different size distributions for Halo 1 (left) and Halo 2 (right) taken at the end of the simulation. These are obtained averaging over the radius within a sphere of 300 kpc, starting from the densest point. See text for details.

Table 1: Specifications of the runs presented in this work: type of distribution, depletion factor $f_{\rm dep}$, dust-to-gas mass ratio $\mathcal{D}$, and type of reverse shock destroying the initial dust distribution. The arrows indicate values above (up) and below (down) the critical $f_{\rm dep}$. We employed $Z_\odot = 0.02$ to be consistent with previous estimates of the $f_{\rm dep}$ (e.g. Pollack et al. 1994). The notation 4.9(-9) reads as 4.9×10^{-9}. Note that the dust-to-gas mass ratio for the power-law distribution has been evaluated as $\mathcal{D} = \mathcal{D}_\odot \times Z/Z_\odot$ with $\mathcal{D}_\odot = 0.00934$ while, as already discussed in the text, for the SN-like distribution we obtain it from the depletion factor as $\mathcal{D} = f_{\rm dep} Z$.

#	type	$f_{\rm dep}$		$\mathcal{D}$	dn/da	shock
run1	no-dust	-	-	0	-	-
run2	35 $M_\odot$	0.0082	$\downarrow$	7.4(-9)	SN model	rev1*
run3	20 $M_\odot$	0.015	$\uparrow$	1.3(-8)	SN model	rev2*
run4	35 $M_\odot$	0.030	$\uparrow$	2.7(-8)	SN model	
run5	35 $M_\odot$	0.10	$\uparrow$	9.0(-8)	SN model	
run6	35 $M_\odot$	0.49	$\uparrow$	4.4(-7)	SN model	
run7	power-law	0.49	$\uparrow$	4.2(-7)	$\alpha = -3.5$	-

* see Chiaki et al. (2014) for details.

also include the dust-to-gas mass ratio obtained from the depletion factor $f_{\rm dep}$ and the metallicity $Z = 4.5 \times 10^{-5} Z_{\odot}$ as $\mathcal{D} = f_{\rm dep} Z$ (see Schneider et al. 2012b). Note that we employ $Z_{\odot} = 0.02$ for consistency with previous work (e.g. Pollack et al. 1994) even if this value is now obsolete (Asplund & Grevesse 2009). It is important however to underline that the estimate of $\mathcal{D}$ as well the value of $Z_{\odot}$ never enter the generation of the tables we have used but we decided to report those to allow for a better comparison with previous investigations.

4. Results

In Fig. 2 we report the averaged thermal evolution for the runs performed for the two halos. In both cases the general trend is very similar, and clearly shows the effect of dust on the thermodynamics. Depending on the employed grain size distribution, we see a weaker or stronger cooling: the runs with low mass dust yield (run2 to run4) start to cool at densities above 10^{-12} g cm^{-3} as a result of the dust cooling and reach a minimum temperature of 800 K, 600 K and 400 K for Halo 1, and 700 K, 500 K and 400 K for Halo 2. When we increase the amount of dust the cooling (H_2 + dust) is much stronger and the effect is already visible at densities of 10^{-18} g cm^{-3}. The minimum temperature reached both in run6 and run7 is around 200 K and could lead to the formation of clumps with masses < 0.01 M$_{\odot}$. The same dust content ($f_{\rm dep} = 0.49$) provides similar results regardless of the choice of the distribution. In fact, assuming a power-law (run7) or a more realistic SN distribution (run6) produces only slight differences of the order of $\sim$50-100 K at densities around $\sim 10^{-13} - 10^{-11}$ g cm^{-3}.

In Fig. 3 we report the H_2 fraction as a function of the density for different runs. As expected from previous studies (e.g. Fig. 4 of Omukai 2000) the H_2 evolution is strongly affected by the presence of dust, in particular it forms more rapidly while $f_{\rm dep}$ is larger than 0.03. This enhanced H_2 fraction results in a slightly higher H_2 cooling as discussed in the next section and also reported by Smith et al. (2015).

To explore and analyze the differences in the thermodynamics in more detail, we report in Fig. 4 results from one-zone models for the most relevant cases. The overall thermal evolution is

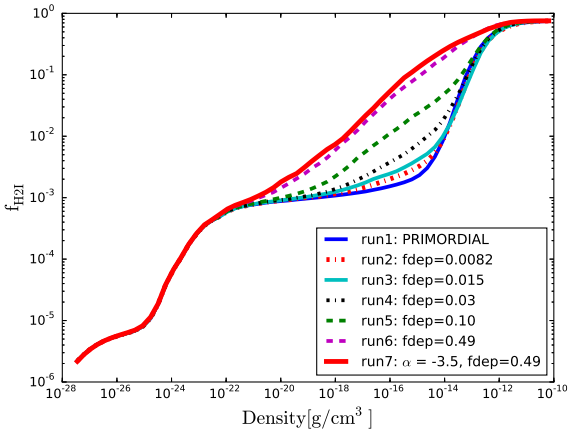

Fig. 3.— Profiles of the mass-weighted average H_2 fraction as a function of the density for the different runs discussed in the text. We report only the results for Halo 1.

in good agreement with the results reported in Fig. 2. In particular the thermal evolution for run6 and run7, which have the same depletion factor $f_{\rm dep} = 0.49$ but different grain-size distributions, looks very similar to our 3D simulations around densities of 10^{-14}-10^{-12} g cm^{-3}, i.e. the cooling provided when employing the grain-size distribution produced by SN models is slightly stronger than the one provided by a Milky Way type distribution only at densities between 10^{-14}-10^{-13} g cm^{-3}. To quantify these differences we plot in Fig. 5 the ratio between the two cooling functions, named $\Lambda_{\rm d}^{\rm MW}$ and $\Lambda_{\rm d}^{\rm SN}$ for the Milky Way and the SN-like distributions, respectively. In the region of densities where the dust cooling becomes relevant the ratio varies from 0.4 to 1.2, which means that the SN distribution provides at most two times more cooling compared to the MW-like distribution. This directly reflects the slight difference in the thermal evolution in Fig. 2 and explains why we do not see dramatic differences on the final results (thermal and dynamical evolution) even if the two distributions are different in size range, composition, and shape. To support our numerical results, we provide in the appendix an analytical derivation for the dust cooling which clearly shows, under the given assumptions, that changing the optical properties and the size of the grains has only minor impact on the final dust cooling.

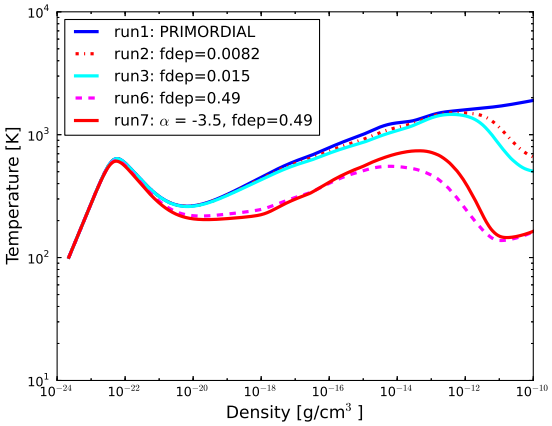

Fig. 4.— Thermal evolution for five specific runs obtained from semi-analytical one-zone models. According to Table 1 we report run1: primordial case, run2 and run3, i.e. the 35 $M_\odot$ and the 20 $M_\odot$ distributions, with $f_{\rm dep}$ 0.0082 and 0.015, respectively, and run6 and run7, that is the SN and the power-law grain-size distributions with the same $f_{\rm dep} = 0.49$.

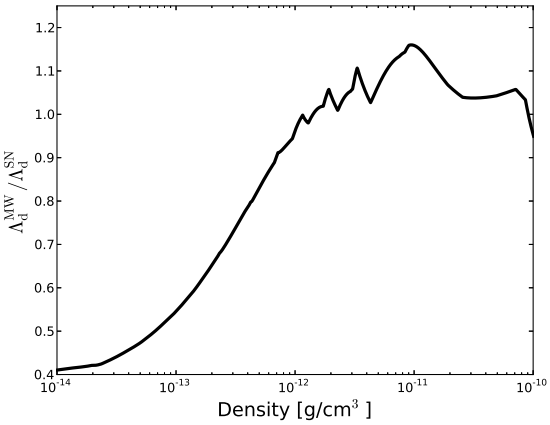

Fig. 5.— Ratio between the cooling $\Lambda_{\rm d}^{\rm MW}$ provided when employing a Milky Way grain-size distribution, and $\Lambda_{\rm d}^{\rm SN}$, i.e. the cooling provided when using the grain-size distribution produced by SN models. Only the relevant density region is shown. This ratio has been calculated from the cooling functions obtained from the one-zone models we performed. Note that the dust cooling linearly scales with the dust mass as shown in the Appendix.

We should add that there are some differences between the thermal evolution obtained from semi-analytical one-zone models and the three-dimensional hydrodynamical simulations, as a consequence of the fact that in 3D the collapse speed is affected by thermal pressure as well by turbulence and rotation. In spite of the agreement in the thermodynamical evolution, we will however show below that the resulting impact on the density structure is different from what was previously assumed in one-zone investigations.

4.1. Conditions for filaments formation

To better understand how the differences in the thermodynamics are reflected in the dynamical evolution, we show in Fig. 6 the density projections along the x-axis for the different runs and the two considered halos, taken at a peak density of 3×10^{-10} g cm^{-3}. The density structure appears very similar in the two halos even if we note more turbulence in Halo 1. When considering the cases with $f_{\rm dep}$ below (run2) or slightly above (run3, run4) the threshold proposed by Schneider et al. (2012b), the collapse proceeds almost monolithically with a turbulent bulky structure which is similar to the primordial case (run1).

When we analyse the cases with a high depletion factor, i.e. $f_{\rm dep} = 0.49$, the gas evolves in a more fragmented and filamentary structure, reflecting the stronger cooling. The relative standard deviation ($RSD = \rho_{\rm rms}/\rho_{\rm mean}$) reported in Fig. 7 confirms that the density dispersion is enhanced when filaments form. The intermediate case with $f_{\rm dep} = 0.10$, which is already one order of magnitude larger than the threshold suggested by semi-analytical models, also shows a compact structure. We can then argue that the dust mass threshold lies in the range $0.10 < f_{\rm dep} \leq 0.49$. A comparison with the thermal evolution further shows that the resulting conditions occur in the regime where $\gamma < 1$, i.e. where the temperature decreases in density. This is consistent with previous results by Peters et al. (2012, 2014) exploring fragmentation in the presence of a fixed equation of state.

To quantitatively assess this point we report in Fig. 8 the most relevant cooling/heating rates as a function of the density for run6, i.e. the run where the dust cooling is very strong. As already discussed in previous works (e.g. see Omukai 2000)

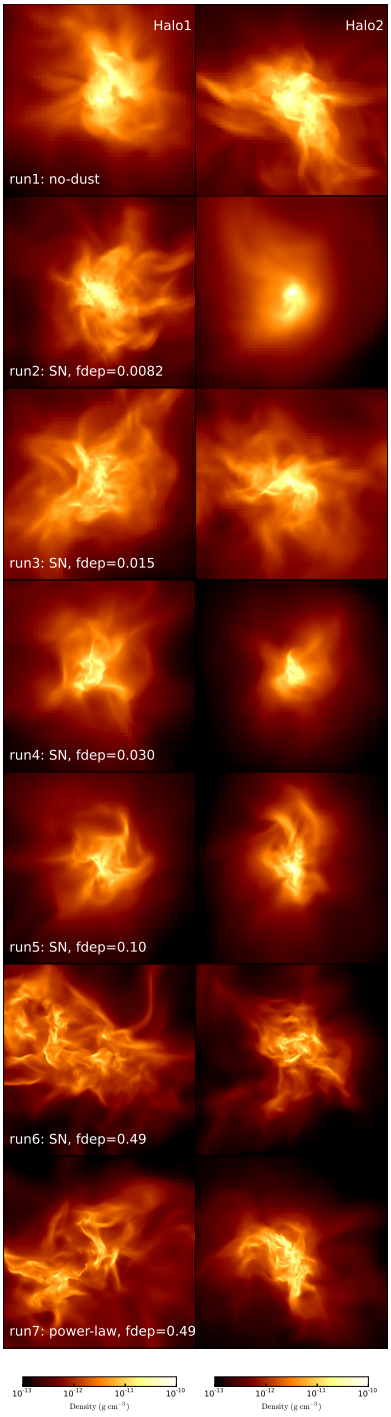

Fig. 6.— Density projections along the x-axis at a scale of 200 AU for the different runs described in Table 1 and the two halos employed in the simulations.

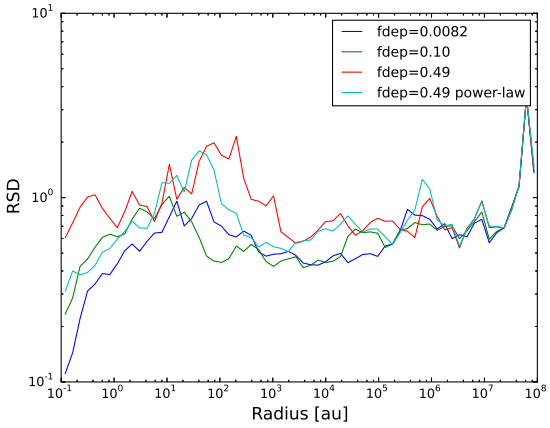

Fig. 7.— Relative standard deviation $\rho_{\rm rms}/\rho_{\rm mean}$ as a function of radius for four different runs with Halo 1 as reported in the legend.

when dust is included both a strong heating due to the catalysis of H_2 on grains as well as an increase of cooling at high densities due to collisions between grain dust and gas occur. The H_2 abundance, as clear from our Fig. 3, is boosted and so the H_2 cooling, at maximum by a factor of two (see also Smith et al. 2015). However this enhancement of H_2 cooling occurs at intermediate densities and it is exceeded by the H_2 formation heating at densities around 10^{-16} g cm^{-3}. This enhanced H_2 cooling could have as an effect to boost the formation of HD as reported by Meece et al. (2014). The only efficient cooling at high densities comes from the dust which is reflected in a sudden drop in the thermal evolution and a $\gamma < 1$. As shown by Peters et al. (2012, 2014), the formation of filaments requires an equation of state with $\gamma < 1$. As evident from our Fig. 8, the latter may occur at densities around 10^{-22}-10^{-20} g cm^{-3}, potentially leading to the formation of high-mass clumps, or at densities above 10^{-14} g cm^{-3} which is well within the dust cooling regime. It should also be noted that Chiaki et al. (2016) discussed the possibility that the heating produced by the H_2 formation on dust grains could sometimes works against fragmentation.

However at this stage of the simulation we are not able to explore the fragmentation process in detail, and it would be important to evolve the system for longer time, following also the subsequent accretion process. Overall, a thin filamen-

tary structure is expected to favour the formation of low-mass stars as clumps are more easily ejected from the filaments reducing the accretion rate, compared for instance to a thick disk case. In a fragmentation mode based on a thick disk, it is conceivable that more material is available for subsequent accretion, and the resulting clumps may be more massive (Clark et al. 2011; Susa et al. 2014; Latif et al. 2015; Stacy et al. 2016). However, we cannot rule out the possibility of three-body ejection events, so that the formation of low-mass stars may also be possible in this context (e.g. see Ji et al. 2014).

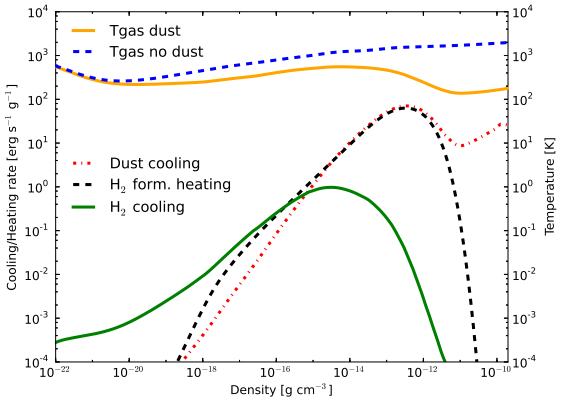

Fig. 8.— Cooling and heating rate as a function of the density for the run with $f_{\rm dep} = 0.49$ (run6 in Table 1) . Only the most relevant contributions are shown, namely the H_2 line cooling, the dust cooling, and the heating due the formation of H_2 both in gas phase and on dust. The thermal evolution is also reported together with the primordial case for reference. Note that the evolution is the same as in Fig. 4 but we focus here on higher densities.

To better understand the effect of the grain-size distribution we look at the case with an increased dust mass for the SN model distribution (run6), reported in Fig. 9. By increasing $f_{\rm dep}$ from 0.0082 to 0.49 we can also catch the effect of the composition/distribution on the thermal evolution and density structure. When comparing the two cases with the same dust content but different distribution and composition (run6 and run7), i.e. different optical properties and size ranges (Fig. 9), we obtain very similar results (see thermal evolution in Fig. 2 and 4) and, in particular, similar fila-

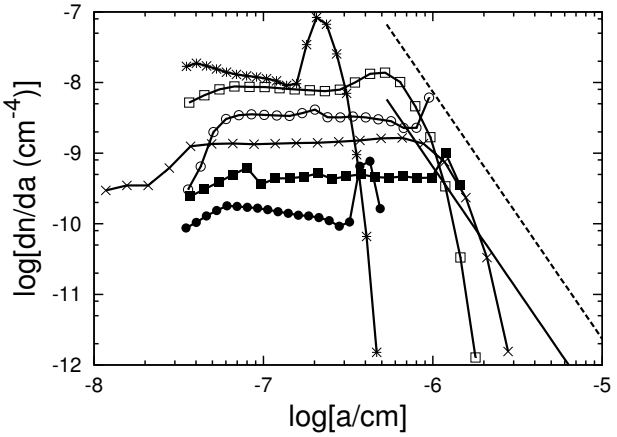

Fig. 9.— Same as figure 1 but for the SN distributions where $f_{\rm dep}$ has been increased to match the dust mass typical of the power-law distribution, i.e. $f_{\rm dep} = 0.49$. Note that the y-scales are different compared to Fig. 1.

mentary density structures (Fig. 6). This crucial result suggests that the grain composition and the shape of the size distribution *do not strongly impact on the evolution of the collapsing halo and its density structure, in particular not as much as the mass yield does*. The latter turns out to be the key physical quantity to understand how Caffau's star was formed.

5. Conclusions and final remarks

In this paper we present 3D hydrodynamical calculations of two collapsing minihalos enriched by dust, starting from cosmological initial conditions. We employ the chemistry package KROME (Grassi et al. 2014) coupled with the hydrodynamical code ENZO including realistic grain size distributions and consistent dust physics. Two different types of grain distributions have been included: i) a standard power-law with composition and dust content similar to our galaxy, i.e. a mix of carbonaceous and silicates, and ii) a more realistic distribution for high-redshift environments (Schneider et al. 2012b). This consists of a sum of log-normal distributions modified by the presence of reverse shocks which flattens the distribution at smaller radii. The two cases allow us to explore different dust compositions and distributions, and assess the effect of the dust physics on the dynamics of the collapsing minihalos. In addition, we ex-

plore one case where the outcome of the SN models has been modified by increasing the dust mass yield, and compare this with the results obtained by employing the standard power-law distribution. We found that the dust mass yield, expressed in terms of the depletion factor $f_{\rm dep}$, is the key quantity which has a strong impact on the dynamical and thermal evolution of the minihalos.

In fact, when we impose the same dust mass (i.e. $f_{\rm dep} = 0.49$) for the standard power-law distribution and the one coming from SN models, these show similar results and dynamical properties. The composition and the size-range, under the conditions explored here and the grain-size distributions employed, are only producing minor differences because of similar dust cooling power. This is also supported by our analytical derivation in the Appendix. In addition, our results suggest that a threshold in dust mass exists, as proposed by Schneider et al. (2012b), but we also found that it is at least one order of magnitude larger. Indeed, the formation of filaments depends more on the equation of state parameter γ (Peters et al. 2012), rather than local minima in the temperature, as often assumed in one-zone investigations. The fragmentation after the formation of such filaments has been investigated in detail by Peters et al. (2014).

Our results then suggest that assuming a single supernova event is not enough to provide the necessary dust mass to induce filaments formation. This leads to other scenarios: i) more than one supernova contributes to the enrichment of the medium and the halo where the star is formed, ii) a weak or no reverse shock should reprocess the dust coming from the SN explosion if a single event is assumed, iii) very efficient grain growth by sticking from the gas phase (in particular on silicates grains) that can increase the dust mass during the collapse should be considered.

However, the latter is rather uncertain as a minimum amount of refractory elements should be present in the gas phase (Chiaki et al. 2014). In addition the grain growth process must be fast enough to increase the depletion factor by orders of magnitudes. Nozawa et al. (2012) provided the conditions under which the grain growth can be efficient, with particular emphasis on the critical refractory elemental abundance needed to growth in function of the initial depletion factor. If we consider the 35 $M_\odot$ case with $f_{\rm dep} = 0.0082$ (run2 in our Table 1), to reach a final $f_{\rm dep}$ of 0.25 (i.e. above the threshold of 0.1 we found) a [Si/H]$\sim$ -4.00 is needed according to Fig. 3 of Nozawa et al. (2012). This is slightly higher compared to the silicon abundance observed in Caffau's star (i.e. [Si/H] = -4.27) and means that grain growth, for this specific case, should not be very efficient. When discussing the above scenarios we should also take into account the uncertainties coming from the dust nucleation models. The formation of dust in SN ejecta in the models included here comes from classical nucleation theory, but other models as the chemical kinetic approach (Cherchneff & Dwek 2009; Biscaro & Cherchneff 2014) may lead to different results (see e.g. Marassi et al. 2015). Also within the same nucleation theory approach, Nozawa et al. (2007) produced different distributions compared to Schneider et al. (2012b) as this strongly depends on the assumptions made in the SN model (see also Chiaki et al. 2015). It is then very important to explore other models which can provide a larger amount of dust under different conditions.

A quantitative and detailed comparison with previous 3D calculations (Dopcke et al. 2011, 2013; Meece et al. 2014; Smith et al. 2015) is difficult to pursue as they employed different dust models and initial setups. Meece et al. (2014) aimed at studying the effect of the metallicity and initial conditions (e.g. spin) on the fragmentation process performing simulations of an idealized halo collapse. However, the maximum density reached in their calculations is $\sim 10^{10}$ cm^{-3} while the dust cooling, for the metallicity explored in this work, starts to be efficient at $n > 10^{11}$ cm^{-3} (i.e. $\rho > 10^{-13}$ g cm^{-3}) as also discussed by Smith et al. 2015. For this reason a direct comparison is not possible. Dopcke et al. (2013) reported temperatures between 200-500 K for metallicities of 10^{-4} - 10^{-5} $Z_\odot$, in line with our results for the power-law distribution, but assuming an average grain size and different optical properties. In Smith et al. (2015) the final temperature reached is slightly higher but the density structure shows similar features as the findings discussed in this work. We further note, that using a realistic depletion factor from the SN models makes a strong difference for the thermodynamics and the dynamical behaviour. We found that the amount of dust

in run3-run5 is below the threshold for which dust cooling becomes relevant. On the other hand, assuming a MW-like distribution/composition, with a high depletion factor, as in the work by Dopcke et al. (2011) and Smith et al. (2015), can lead to an overcooling.

When discussing fragmentation processes it is also important to consider not only the thermodynamics, but also the dynamical processes which can change the picture sketched here. In particular, it is clear that supernovae can change the density structure and thus the initial conditions for star formation. In case of external enrichment in a scenario as modeled by Smith et al. (2015), the resulting impact may be weaker, as the strength of the supernova shock has already decreased when reaching the new halo, and they also reported that the new material has efficiently mixed with the existing one, providing relatively uniform initial conditions. A more pronounced effect may occur when considering fall-back from supernovae that exploded within the same halo (see Ritter et al. 2012 and Cooke et al. 2014 in the context of carbon-enhanced metal poor stars). Such a scenario may have a stronger effect on the remaining mass that is still available for the process of star formation. We however note that in any case the material has to reach at least a Jeans mass if star formation is to occur, so that subsequently a homologous collapse may occur. From the comparison of our one-zone models with the 3D simulations, we expect no strong differences regarding the thermal evolution, even though the outcome with respect to fragmentation may certainly depend on the mass that was initially available. Recently, Hopkins & Conroy (2015) introduced the so called "promoted star formation" mechanism, which can be activated even in minihalos where the total metallicity is low, but a locally high dust mass could exist due to fluctuations induced by the dust dynamics. This model assumes that the dust distribution and composition in the early Universe is the same as the one observed for our galaxy.

In addition, considering that this star is a very rare object it could also be that it has been formed from specific uncommon dynamical conditions, as for instance halos with very high spin as the ones reported by de Souza et al. (2013) and Stacy et al. (2014) even if in the recent calculations by Meece et al. (2014) this seems unlikely to affect the collapse.

To conclude, the results presented in this work provide a relevant step forward to understand the main dust uncertainties and the parameters influencing the dynamical evolution of low-metallicity collapsing halos.

Acknowledgments

SB, DRGS, and RB thank for funding through the DFG priority program "The Physics of the Interstellar Medium" (projects BO 4113/1-2, SCHL 1964/1-2, and BA 3706/3-2). TG acknowledges the Centre for Star and Planet Formation funded by the Danish National Research Foundation. DRGS thanks for funding through Fondecyt regular (project code 1161247) and through the "Concurso Proyectos Internacionales de Investigación, Convocatoria 2015" (project code PII20150171). SB also acknowledges the kind hospitality of the Kavli Institute for Theoretical Physics (KITP) where this work has been completed, and Andrea Ferrara, Troels Haugbølle, and Raffaella Schneider, for fruitful discussions on this topic. We are indebted to Hiroyuki Hirashita for the derivation of the equations reported in the Appendix. This research was supported in part by the National Science Foundation under Grant No. NSF PHY11-25915. The plots of this paper have been obtained by using the YT tool (Turk et al. 2011). The simulations have been performed on the German HLRN cluster under the project nip00035.

REFERENCES

Asplund, M. and Grevesse, N. and Sauval, A. J. and Scott, P., 2009, ARA&A, 47, 481

Biscaro, C., & Cherchneff, I. 2014, A&A, 564, A25

Bovino, S., Grassi, T., Latif, M. A., & Schleicher, D. R. G. 2013, MNRAS, 434, L36

Bovino, S., Grassi, T., Schleicher, D. R. G., & Latif, M. A. 2014, ApJ, 790, L35

Bromm, V., Ferrara, A., Coppi, P. S., & Larson, R. B. 2001, MNRAS, 328, 969

Bryan, G. L., Norman, M. L., O'Shea, B. W., et al. 2014, ApJS, 211, 19

Caffau, E., Bonifacio, P., François, P., et al. 2011, Nature, 477, 67

Cazaux, S., & Spaans, M. 2009, A&A, 496, 365

Cen, R. 1992, ApJS, 78, 341

Cherchneff, I., & Dwek, E. 2009, ApJ, 703, 642

Chiaki, G., Schneider, R., Nozawa, T., et al. 2014, MNRAS, 439, 3121

Chiaki, G., Marassi, S., Nozawa, T. et al. 2015, MNRAS, 446, 2659

Chiaki, G., Yoshida, N., & Hirano, S. 2016, arXiv:1601.00280

Clark, P. C., Glover, S. C. O., Smith, , R. J., et al. 2011, Science, 331, 1040

Cooke, R. J., & Madau, P. 2014, ApJ, 791, 116

de Souza, R. S., Ciardi, B., Maio, U. and Ferrara, A., S. 2013, 428, 2109

Dopcke, G., Glover, S. C. O., Clark, P. C., & Klessen, R. S. 2011, ApJ, 729, L3

—. 2013, ApJ, 766, 103

Draine, B. T. & Lee, H. M., 1984, ApJ, 285, 89

Federrath, C., Sur, S., Schleicher, D. R. G., Banerjee, R., & Klessen, R. S. 2011, ApJ, 731, 62

Glover, S. C. O. 2015, MNRAS, 451, 2082

Grassi, T., Bovino, S., Haugbølle, T., & Schleicher, D. R. G. 2016, MNRAS, accepted, arXiv:1606.01229

Grassi, T., Bovino, S., Schleicher, D. R. G., et al. 2014, MNRAS, 439, 2386

Hirano, S., Hosokawa, T., Yoshida, N., et al. 2014, ApJ, 781, 60

Hollenbach, D., & McKee, C. F. 1979, ApJS, 41, 555

—. 1989, ApJ, 342, 306

Hopkins, P. F., & Conroy, C. 2015, arXiv:1512.03834

Ji, A. P., Frebel, A., & Bromm, V. 2014, ApJ, 782, 95

Katz, H., Sijacki, D., & Haehnelt, M. G. 2015, MNRAS, 451, 2352

Klessen, R. S., & Glover, S. C. O. 2014, arXiv: 1412.5182

Klessen, R. S., Glover, S. C. O., & Clark, P. C. 2012, MNRAS, 421, 3217

Lagache, G., Abergel, A., Boulanger, F., Désert, F. X., Puget, J.-L., 1999, A&A, 344, 322

Latif, M. A., Schleicher, D. R. G., Schmidt, W., Niemeyer, J. 2013, ApJ, 772, L3

Latif, M. A., Bovino, S., Van Borm, C., et al. 2014, MNRAS, 443, 1979

Latif, M. A., Omukai, K., Habouzit, M., Schleicher, D. R. G., & Volonteri, M. 2016, ApJ, 823, 40

Limongi, M., & Chieffi, A. 2012, ApJS, 199, 38

Marassi, S., Schneider, R., Limongi, M., et al. 2015, MNRAS, 454, 4250

Mathis, J. S., Rumpl, W., & Nordsieck, K. H. 1977, ApJ, 217, 425

Mayer, M., & Duschl, W. J. 2005, MNRAS, 358, 614

Meece, G. R. and Smith, B. D. and O'Shea, B. W., 2014, ApJ, 783, 75

Nozawa, T., Kozasa, T., & Habe, A. 2006, ApJ, 648, 435

Nozawa, T., Kozasa, T., Habe, A., et al. 2007, ApJ, 666, 955

Nozawa, T., Kozasa, & Nomoto, K. 2012, ApJ, 756, L35

Omukai, K. 2000, ApJ, 534, 809

Peters, T., Schleicher, D. R. G., Klessen, R. S., et al. 2012, ApJ, 760, L28

Peters, T., Schleicher, D. R. G., Smith, R. J., Schmidt, W., Klessen, R. S., 2014, MNRAS, 442, 3112

Pollack, J. B., Hollenbach, D., Beckwith, S., et al. 1994, ApJ, 421, 615

Prieto, J., Jimenez, R., Haiman, Z., & González, R. E. 2015, MNRAS, 452, 784

Ritter, J. S., Safranek-Shrader, C., Gnat, O., Milosavljević, M., Bromm, V. 2012, ApJ, 761, 56

Safranek-Shrader, C., Milosavljević, M., & Bromm, V. 2014, MNRAS, 440, L76

Schady, P., Page, M. J., Oates, et al. 2010, MNRAS, 401, 2773

Latif, M. A., & Schleicher, D. R. G. 2015, MNRAS, 449, 77

Schleicher, D. R. G., Bovino, S., Latif, M. A., Ferrara, A., & Grassi, T. 2016, A&A, 585, A11

Schneider, R., Omukai, K., Bianchi, S., & Valiante, R. 2012a, MNRAS, 419, 1566

Schneider, R., Omukai, K., Inoue, A. K., & Ferrara, A. 2006, MNRAS, 369, 1437

Schneider, R., Omukai, K., Limongi, M., et al. 2012b, MNRAS, 423, L60

Seifried, D., & Walch, S. 2016, MNRAS, 459, L11

Smith, B. D., Wise, J. H., O'Shea, B. W., Norman, M. L., & Khochfar, S. 2015, MNRAS, 452, 2822

Stacy, A., & Bromm, V. 2014, ApJ, 785, 73

Stacy, A., Bromm, V., & Lee, A. T., 2016, arXiv: 1603.09475

Susa, H., Hasegawa, K., & Tominaga, N., 2014, ApJ, 792, 32

Todini, P., & Ferrara, A. 2001, MNRAS, 325, 726

Truelove, J. K., Klein, R. I., McKee, C. F., et al. 1997, ApJL, 489, L179

Turk, M. J., Smith, B. D., Oishi, J. S., et al. 2011, ApJS, 192, 9

Zafar, T. and Møller, P., Ledoux, C., et al. 2011, A&A, 532, A51

This 2-column preprint was prepared with the AAS LaTeX macros v5.2.

A. Impact of optical properties, size, and mass on the dust cooling

If we make some assumptions on the thermal balance equation for the dust-gas interaction (Eq. 4), we can disentangle the effect of the size, the mass, and the optical properties on the dust cooling from analytical considerations. First of all let us consider Eq. 4 in the optically thin regime, i.e. $\beta_e(\mathbf{T}_d) = 1$, and neglect the effect of the absorption from the CMB, i.e. all the $\Gamma_{abs,i} = 0$, considering the interaction gas-grains more efficient than the absorption of UV and visible radiation, which is reasonable in high-density regime. We simply have for the global system that the energy absorbed by the interaction with the gas equates the thermal emission of infrared photons by the grains

$$\Gamma_{em} = \Lambda_{dust} \tag{A1}$$

which is

$$\int_0^\infty \int_0^\infty 4\pi\kappa_\nu B_\nu(T_d) m_d \varphi(a) da d\nu = \int_0^\infty \pi a^2 n_g v_g 2k_B(T - T_d)\varphi(a) da. \tag{A2}$$

We neglect here the dependency of T_d from the size. The terms in the above equation are described in Table 2. We can relate the Planck mean opacity to the absorption coefficient Q_{abs} through the following equation

$$\kappa_\nu = \frac{Q_{abs}\pi a^2}{m_d}, \tag{A3}$$

which becomes

$$\kappa_\nu = \frac{3}{4}\frac{Q_{abs}}{a\rho_0}, \tag{A4}$$

with ρ_0 being the bulk density of a grain (e.g. 2.3 for graphite, see Nozawa et al. 2006) and Q_{abs} being the dimensionless absorption coefficient defined as the ratio between the absorption cross section and the surface area of the grain $Q_{abs} = \sigma_{abs}/(\pi a^2)$.

Under the assumption of instantaneous thermal equilibrium, the solution of eq. A2 allows us to obtain the dust temperature. In this specific case we will analyse the right-hand side (RHS) and the left-hand side (LHS) separately. Due to the fact that we neglect the dependency of T_d from the size, we can split the two integrals on the LHS as

$$4\pi\frac{4}{3}\pi\rho_0 \int_0^\infty \kappa_\nu B_\nu(T_d) d\nu \int_0^\infty a^3 \varphi(a) da. \tag{A5}$$

After integration over the black-body spectrum and defining the absorption efficiency in the mid-infrared as approximately $\kappa_\nu = \kappa_0(\nu/\nu_0)^\beta$ we obtain

$$4\pi\frac{4}{3}\pi\rho_0\kappa_0 C T_d^{4+\beta}\langle a^3\rangle n_d, \tag{A6}$$

where C is a constant factor coming from the integration of the black-body function and has units of erg cm^{-2} K$^{-(4+\beta)}$ s^{-1}, $\langle a^3\rangle$ represents the average over the the grain-size distribution $\varphi(a)$, with $\int_0^\infty \varphi(a)da = n_d$, and β usually ranges between 1-2[6], with ν_0 being a reference frequency. We can re-write the above equation in function of the dust mass density $\rho_d = n_d m_d$ to get the final expression for the LHS term

[6]The value of the exponent depends upon the nature of the grain, but some observational constraints have been proposed by using the spectral energy distribution of the emitted radiation, see for example Lagache et al. (2012).

$$4\pi\frac{4}{3}\pi\rho_0\kappa_0 C T_d^{4+\beta}\langle a^3\rangle\rho_d\frac{3}{4}\frac{1}{\pi\rho_0\langle a^3\rangle}. \tag{A7}$$

The resulting cooling rate obtained from the LHS term under the assumption of thermal equilibrium is

$$\Gamma_{em} \equiv \Lambda_d^{lhs} = 4\pi C\kappa_0 T_d^{4+\beta}\rho_d. \tag{A8}$$

The RHS after integration over the size distribution is simply

$$\pi\langle a^2\rangle n_g v_g n_d 2k_B(T - T_d), \tag{A9}$$

and introducing the dust mass density we get the final expression

$$\Lambda_{dust} \equiv \Lambda_d^{rhs} = \frac{3}{2}\frac{\langle a^2\rangle}{\langle a^3\rangle} n_g v_g k_B (T - T_d)\frac{\rho_d}{\rho_0}. \tag{A10}$$

Equating equation A8 and A10, the solution of which is T_d, we obtain

$$\frac{T - T_d}{T_d^{4+\beta}} = \frac{8}{3}\frac{\pi\rho_0 C\kappa_0}{n_g v_g k_B}\frac{\langle a^3\rangle}{\langle a^2\rangle}. \tag{A11}$$

In the limit of very high densities ($n_g > 10^{12}$ cm^{-3}), where the dust cooling becomes important, T_d and T are almost coupled, and we can assume $T = T_d + \epsilon$, with ϵ being a small number. Equation A11 can be approximated to

$$T_d^{4+\beta} = \frac{3}{8}\frac{n_g v_g k_B \epsilon}{\pi\rho_0 C\kappa_0}\frac{\langle a^2\rangle}{\langle a^3\rangle}. \tag{A12}$$

Note that ϵ slightly changes during the evolution but we can in practice consider it as constant for our analysis. Combining equations A8, A10, and A12 allows us to make the following considerations given that the LHS and the RHS of Eq. A12 must be equal:

- T_d is independent on the dust mass density ρ_d. The only effect of the dust mass is to linearly increase both the LHS (Eq. A8) and the RHS (Eq. A10) terms by the same amount. Generally speaking the dust cooling increases when the dust mass increases. As $\rho_d = \mathcal{D}\rho_g = f_{\rm dep} Z/Z_\odot \rho_g$, in terms of depletion factor the dust cooling linearly increases with increasing $f_{\rm dep}$ as also shown by our numerical simulations.

- Fixing the size a: if κ_0 increases, i.e. the emissivity capacity of a grain increases, T_d only slightly decreases because of the strong dependence $\sim T_d^{4+\beta}$. This means that in Eq. A8 κ_0 and $T_d^{4+\beta}$ almost compensate each other and the net effect is a slight change in the cooling. In general changing the dust composition has a relative small effect on the cooling function.

- Fixing the composition, i.e. κ_0: if $\langle a^3\rangle/\langle a^2\rangle$ in Eq. A12 increases, i.e. we have an increase in the size a, again T_d slightly decreases because physically the volume available to the grain to emit radiation increases ($\Gamma_{em} \propto a^3$) relatively to the dust heating which is proportional to the surface $\propto a^2$. This means that $\langle a^2\rangle/\langle a^3\rangle$ in Eq. A10 decreases, but the dust cooling is slightly affected due again to the compensation between the size-term and the dust temperature term.

To conclude from our simple analytical analysis, it is clear that the optical properties as well as the size do not strongly affect the final dust cooling unless they change by many orders of magnitudes. The only key quantity which linearly affects the cooling is the dust mass as also shown by our numerical simulations.

quantities	symbol	formula	units
Gas temperature	T	-	K
Boltzmann constant	k_B	-	erg K^{-1}
Dust temperature	T_d	-	K
Dust bulk density	ρ_0	-	g cm^{-3}
Dust size	a	-	cm
Dust-to-gas mass ratio	$\mathcal{D}$	$\frac{\rho_d}{\rho_g}$	-
Dust mass	m_d	$\frac{4}{3}\pi a^3 \rho_0$	g
Metals mass in gas phase	m_Z	-	g
Depletion factor	$f_{\rm dep}$	$\frac{m_d}{m_d+m_Z}$	-
Dust number density	n_d	-	cm^{-3}
Dust mass density	ρ_d	$n_d m_d$	g cm^{-3}
Dust opacity	κ_ν	$\kappa_0(\frac{\nu}{\nu_0})^\beta$	cm^2 g^{-1}
Dust distribution	$\varphi(a)$	$\frac{dn_d}{da}$	cm^{-4}
Black-body spectrum	B_ν	$\frac{2h\nu^3}{c^2}\frac{1}{\exp\frac{h\nu}{k_B T_d}-1}$	erg cm^{-2} sr^{-1} s^{-1} Hz^{-1}

Table 2: Symbols and mathematical expressions of the quantities used in the appendix. The units are also reported in column 4th.